Auxiliary materials for

Tomography of the 2011 Iwaki earthquake (M 7.0) and Fukushima nuclear power plant area

Ping Tong[1,2], Dapeng Zhao[1] and Dinghui Yang[2]

[1] {Department of Geophysics, Tohoku University, Sendai 980-8578, Japan}

[2] {Department of Mathematical Sciences, Tsinghua University, Beijing, China}

Correspondence to: P. Tong (tongping85@gmail.com)

D. Zhao (zhao@aob.gp.tohoku.ac.jp)

1 Resolution tests

We conducted checkerboard resolution tests to confirm the reliability of the obtained tomographic images. To make a checkerboard, we assigned alternative positive and negative velocity anomalies of 6% to all the 3-D grid nodes. Random errors with a standard deviation of 0.1 s were added to the synthetic arrival times calculated for the checkerboard model to account for the picking errors existing in the real data.

Figs. S1 and S2 show the finite-frequency results of the checkerboard tests at four layers in the crust under the area where the 2011 Iwaki earthquake occurred and the Fukushima nuclear power plant (FNPP) is located for the Vp and Vs structures, while Figs. S3 and S4 show the finite-frequency results at four layers in the upper mantle beneath the whole study area. The corresponding test results with the ray tomography method (Zhao et al., 1992) are demonstrated in Figs. S5-S8. Although the resolution is lower at 12.0 km depth, the results of resolution tests indicate that the two tomographic methods can well resolve the heterogeneities in the Iwaki earthquake and FNPP area. To further demonstrate the recovery ability of the tomographic methods, we adopted the structural similarity (SSIM) index (Tong et al., 2011) to quantitatively measure the recovery rate of synthetic test with respect to the checkerboard model. For both the finite-frequency and ray tomography methods, Table S1 shows the SSIM indices between the input checkerboard model and the inversion results at different depths. Each index in this table corresponds to one subfigure in Figs. S1-S8. The SSIM indices indicate that the data set used in this study guarantees satisfactory recovery rates for both tomographic methods.

2 Ray and finite-frequency tomographic images

For the finite-frequency traveltime tomography, it is important to correctly compute the sensitivity kernels. Since the band-limited sensitivity kernels in homogeneous media or smoothly heterogeneous media are very close to those of the dominant frequency, it is valid to construct the finite-frequency traveltime sensitivity kernels at the dominant frequencies (e.g., Dahlen et al., 2000; Liu et al., 2009). Similar to our previous work (Tong et al., 2011), the P-wave dominant frequencies are directly determined by using the approximate relation between the corner frequency f_c^P and magnitude M as follows,

$$f_c^P = 105.3614 \times 10^{-0.4712M} . \tag{S1}$$

The dominant frequencies of the S-wave are calculated by using a similar relation as

$$f_c^S = 98.3216 \times 10^{-0.4729M} . \tag{S2}$$

The approximate relations (S1) and (S2) are determined by analyzing the displacement spectra of local earthquakes as that in our previous study (Tong et al., 2011). Using the regressive relation between the dominant frequency and earthquake magnitude (equation

S1 or S2), we can directly estimate the dominant frequency from the magnitude for each earthquake, and compute the sensitivity kernel for the dominant frequency.

The finite-frequency results of the crustal Vp and Vs tomography at four representative layers in the Iwaki earthquake and FNPP area are shown in Figs. 3 and 4. The corresponding results of ray tomography are demonstrated in Figs. S9 and S10. Strong lateral heterogeneities are revealed in the study area (Figs. 3 and 4, Figs. S9 and S10). The 2011 Iwaki mainshock (M 7.0) and its large aftershocks (M > 5.0) are located in a boundary zone with strong variations in seismic velocities. Low-velocity (low-V) anomalies are noticeable in the upper crust in and around FNPP.

Comparing Figs. 3 and 4 with Figs. S9 and S10, we can see that the finite-frequency and ray tomography methods have generated nearly the same velocity images. The only difference is that the finite-frequency results exhibit slightly higher amplitudes of velocity perturbations, which was also found by the previous studies (e.g., Gautier et al., 2008; Tong et al., 2011). The consistency of the tomographic results generated by the two different methods is quantitatively verified by the SSIM indices between the two tomographic models at different depths (Table S2).

Figs. S11 and S12 display the vertical cross-sections of tomography along different profiles with the ray tomography method. The corresponding finite-frequency images are shown in Figs. 5 and 6. Similar to the map views (Figs. 3 and 4, Figs. S9 and S10), the overall patterns of tomography in the vertical cross-sections generated by the finite-frequency and ray tomography methods are nearly the same.

Figure S13 shows an example of P and S wave finite-frequency travel-time sensitivity kernels with a dominant frequency of 4.0 Hz in a velocity model that includes the subducting Pacific slab and the Conrad and Moho discontinuities have lateral depth variations (Zhao et al., 1992).

Auxiliary References

Dahlen, F.A., Hung, S.H., and Nolet, G.: Frechet kernels for finite-frequency traveltimes-I. Theory, *Geophys. J. Int.*, 141, 157-174, 2000.

Gautier, S., Nolet, G., and Virieux, J.: Finite-frequency tomography in a crustal environment: Application to the western part of the Gulf of Corinth, Geophys. Prospect., 56, 493-503, 2008.

Liu, Y., Dong, L., Wang, Y., Zhu, J., and Ma, Z.: Sensitivity kernels for seismic Fresnel volume tomography, *Geophys.*, 74, U35-U46, 2009.

Tong, P., Zhao, D., and Yang, D.: Tomography of the 1995 Kobe earthquake area: comparison of finite-frequency and ray approaches, Geophys. J. Int., 187, 278-302, 2011.

Zhao, D., Hasegawa, A., and Horiuchi, S.: Tomographic imaging of P and S wave velocity structure beneath northeastern Japan, J. Geophys. Res., 97, 19,909-19,928, 1992.

Table S1: Structural similarity (SSIM) indices between the checkerboard model and the inversion result at different depths for P-wave and S-wave tomography. In the crust (at the depths of 6.0, 12.0, 20.0 and 30.0 km), the SSIM indices are calculated in the Iwaki earthquake and Fukushima nuclear power plant area; while in the upper mantle (at the depths of 40.0, 60.0, 90.0 and 120.0 km), they are calculated for the entire study region. The inversion results are obtained by using finite-frequency tomography (FFT) or ray approach.

Depth (km)	6.0	12.0	20.0	30.0	40.0	60.0	90.0	120.0
FFT: P-wave	0.8323	0.7146	0.9634	0.9614	0.9109	0.9478	0.9211	0.7961
Ray: P-wave	0.8664	0.6969	0.8859	0.9728	0.9462	0.9558	0.9347	0.8156
FFT: S-wave	0.8593	0.7641	0.9589	0.9663	0.9400	0.9693	0.9462	0.8367
Ray: S-wave	0.8480	0.6859	0.8836	0.9578	0.9385	0.9639	0.9445	0.8289

Table S2: Structural similarity (SSIM) indices between the finite-frequency and ray tomography results at different depths under the whole study area.

Depth (km)	6.0	12.0	20.0	30.0	40.0	60.0	90.0	120.0
P-wave	0.9628	0.9642	0.9555	0.9908	0.9331	0.9661	0.9847	0.9926
S-wave	0.9745	0.9696	0.9742	0.9868	0.9682	0.9758	0.9937	0.9970

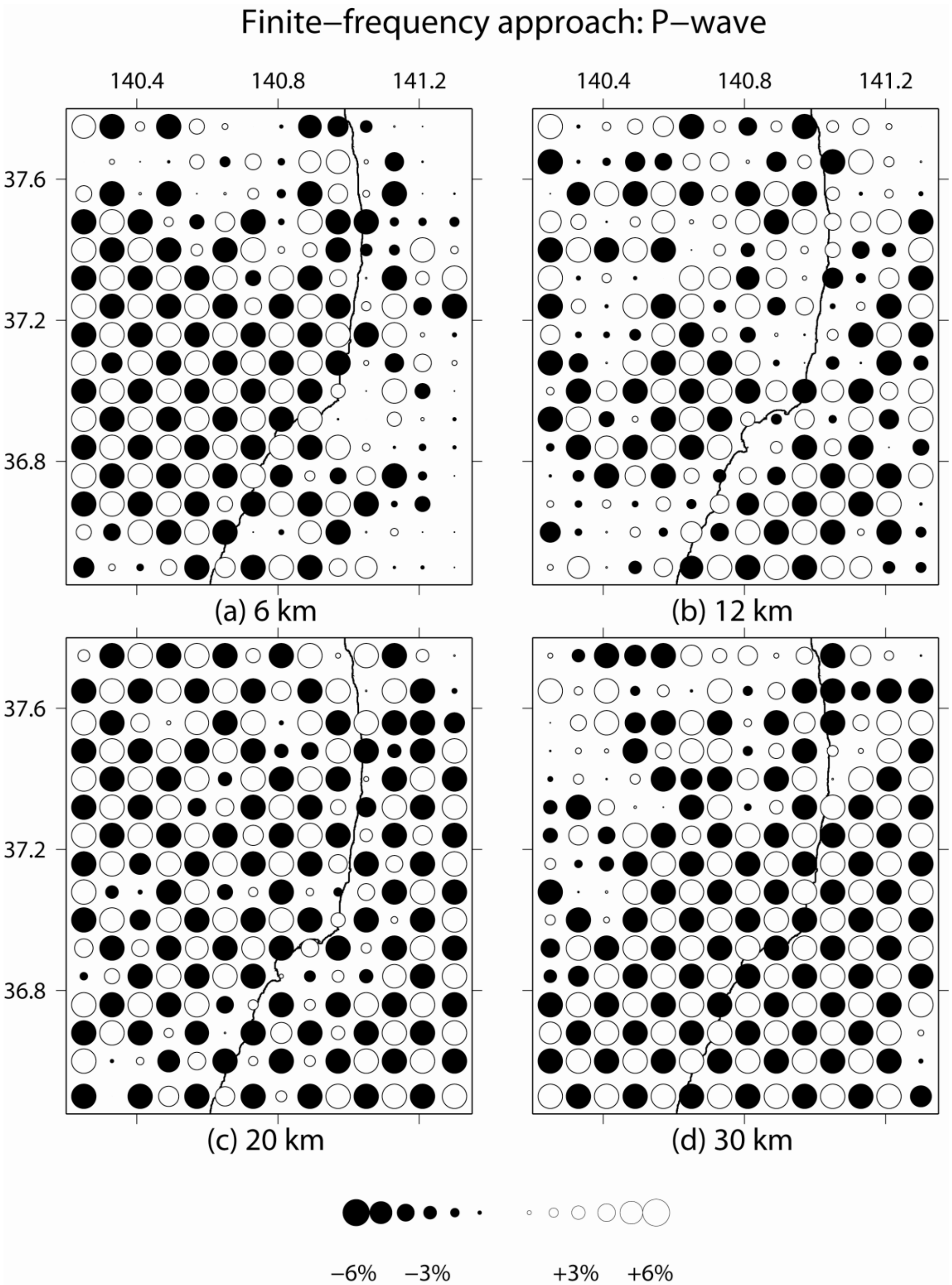

108

109 Figure S1. Finite-frequency results of a checkerboard resolution test for Vp structure at

110 four representative depth layers in the crust under the Iwaki earthquake and the

111 Fukushima nuclear power plant area.

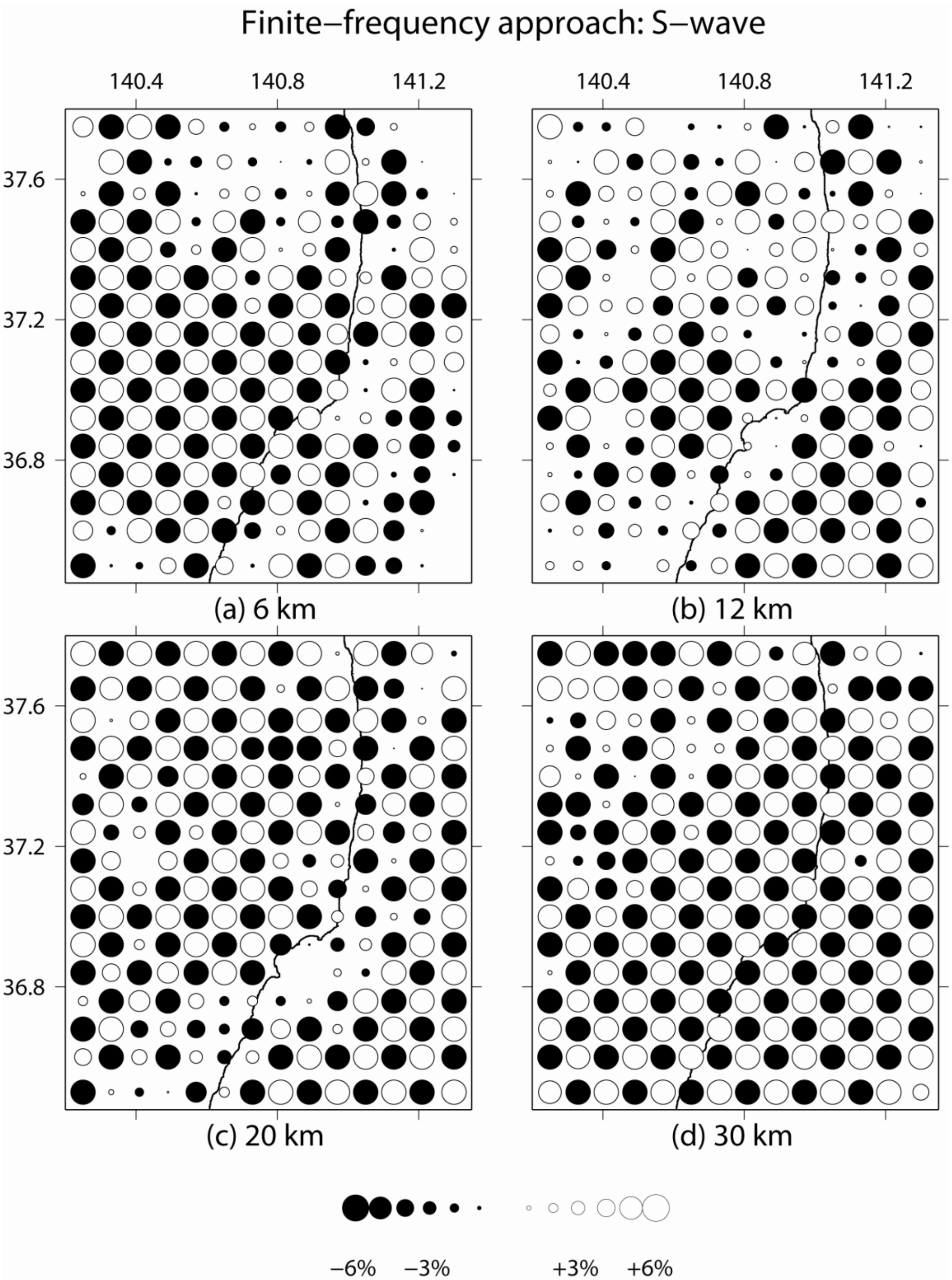

Figure S2. The same as Fig. S1 but for Vs structure.

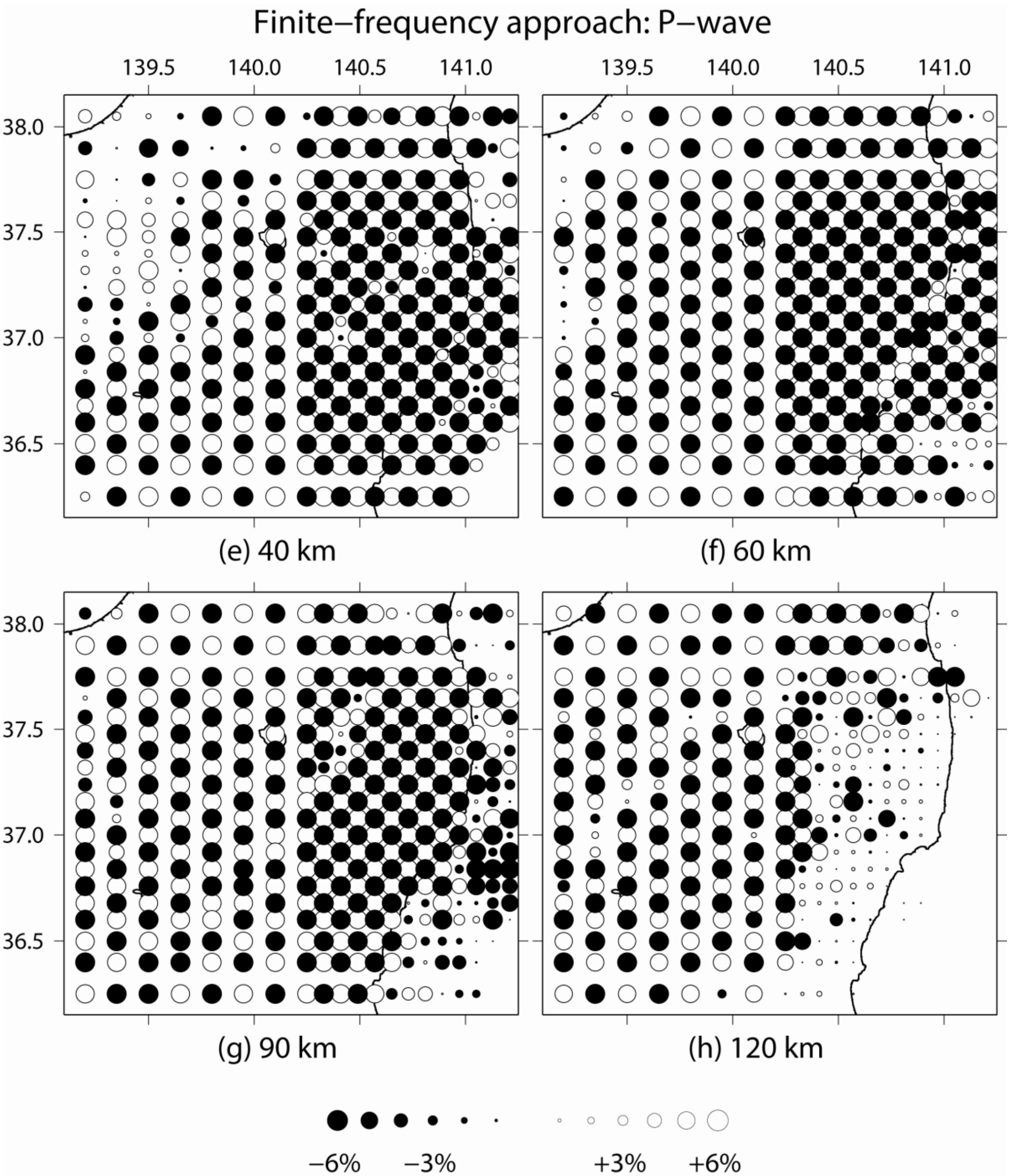

116

117 Figure S3. Finite-frequency results of a checkerboard resolution test for Vp structure at

118 four representative depth layers in the upper mantle under the whole study area.

119

120

121

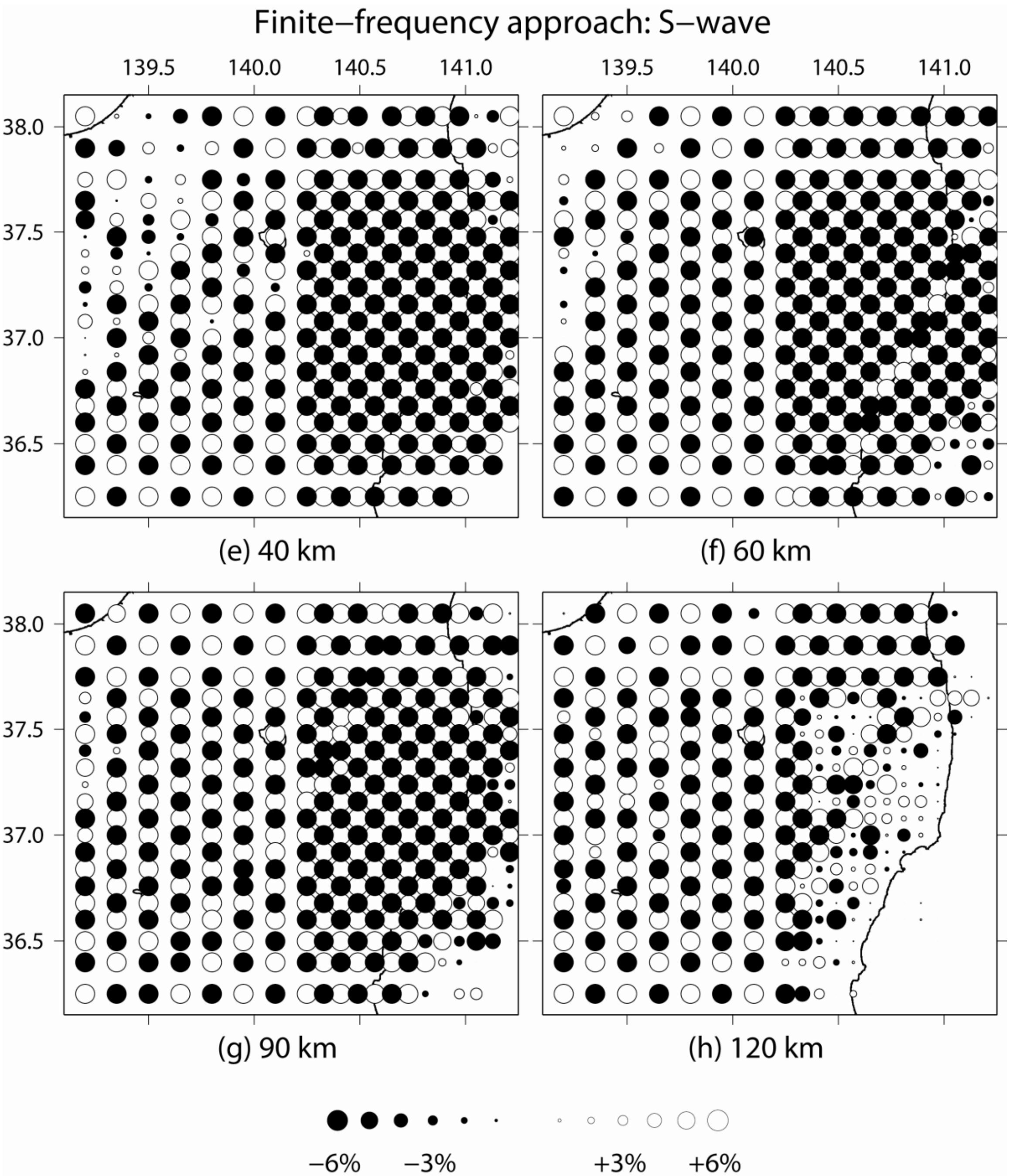

122

123 Figure S4. The same as Fig. S3 but for Vs structure.

124

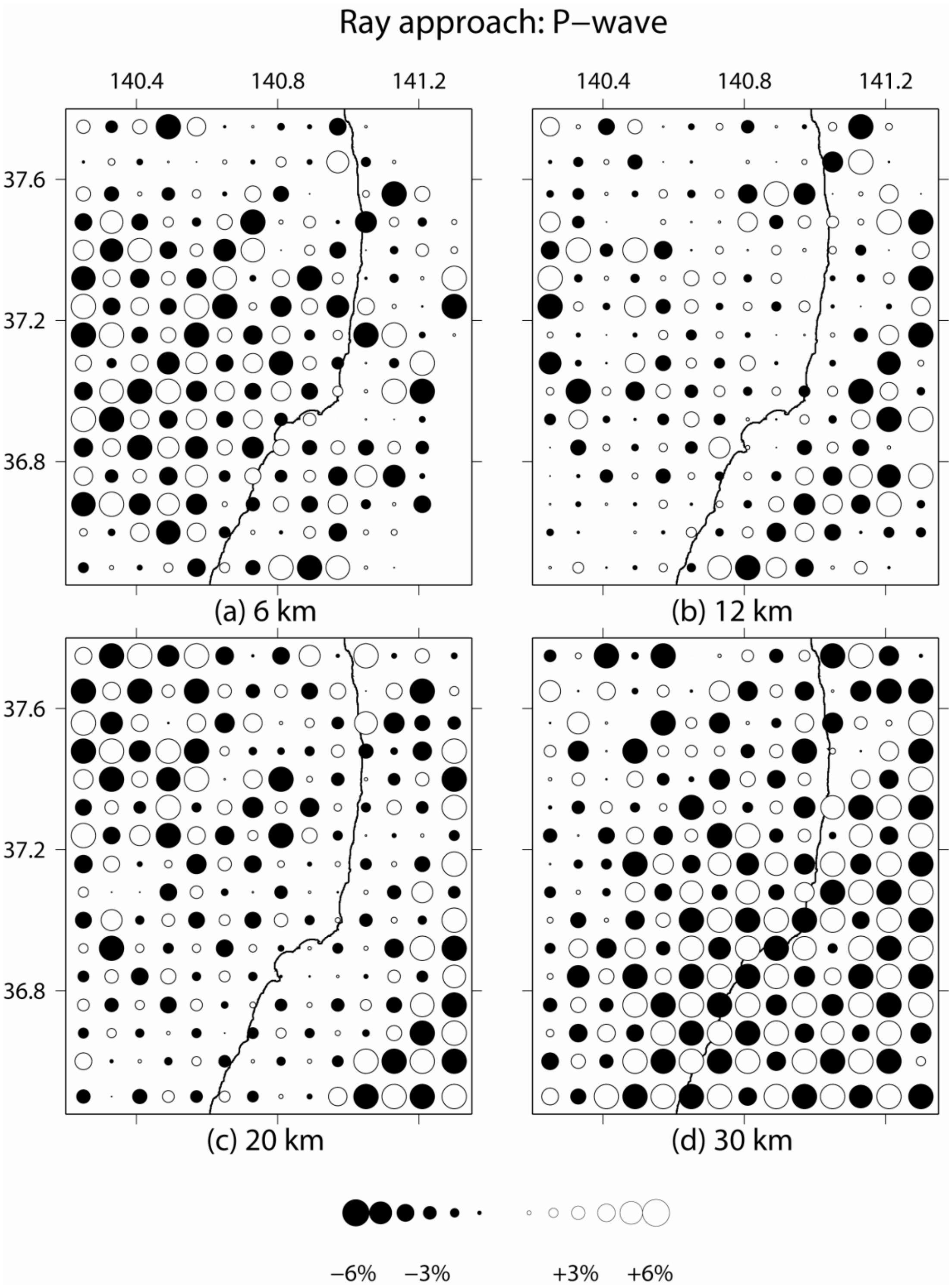

Figure S5. Ray approach results of a checkerboard resolution test for Vp structure at four representative depth layers in the crust under the Iwaki earthquake and the Fukushima nuclear power plant area.

129 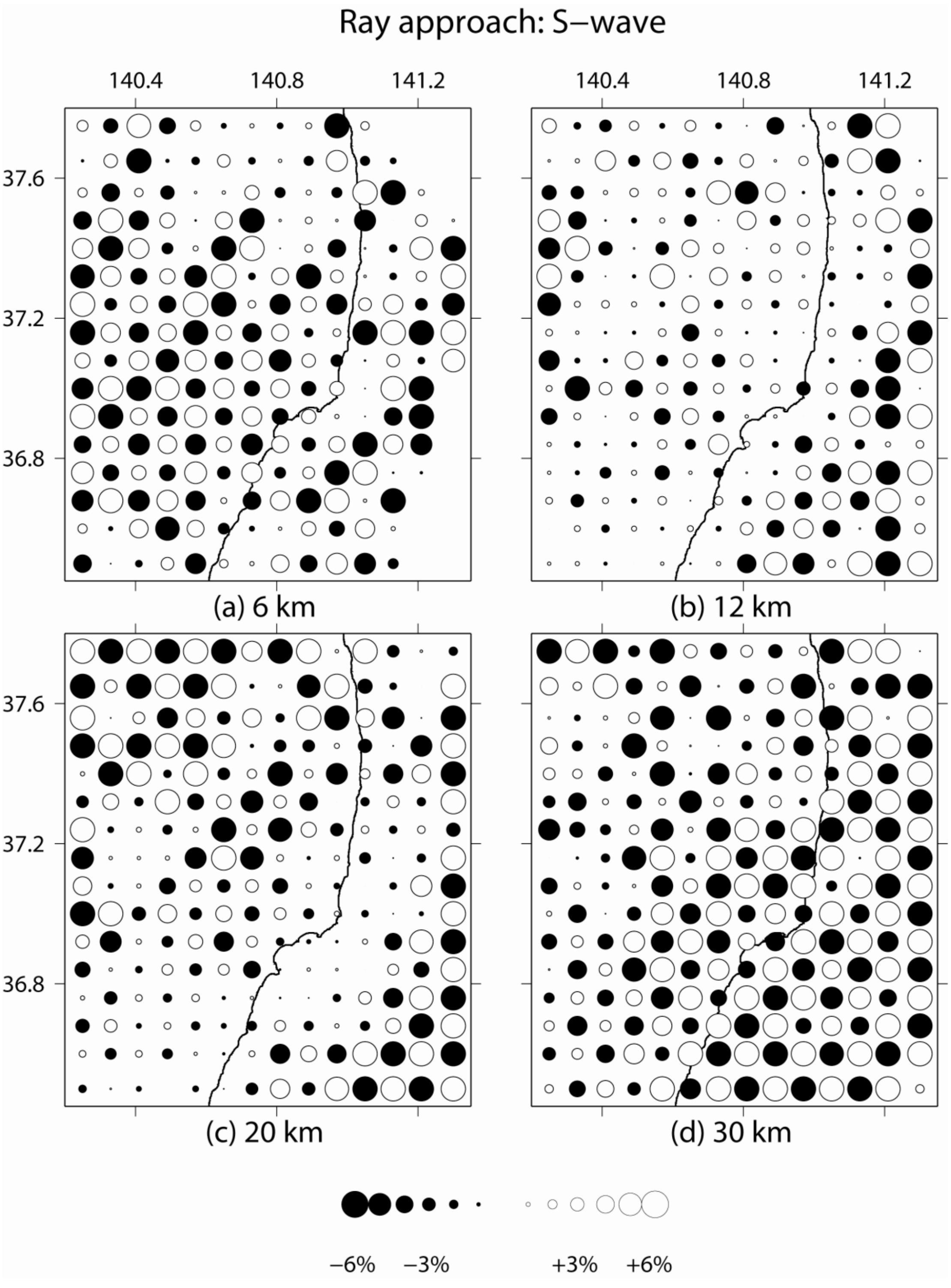

130 Figure S6. The same as Fig. S5 but for Vs structure.

131

132

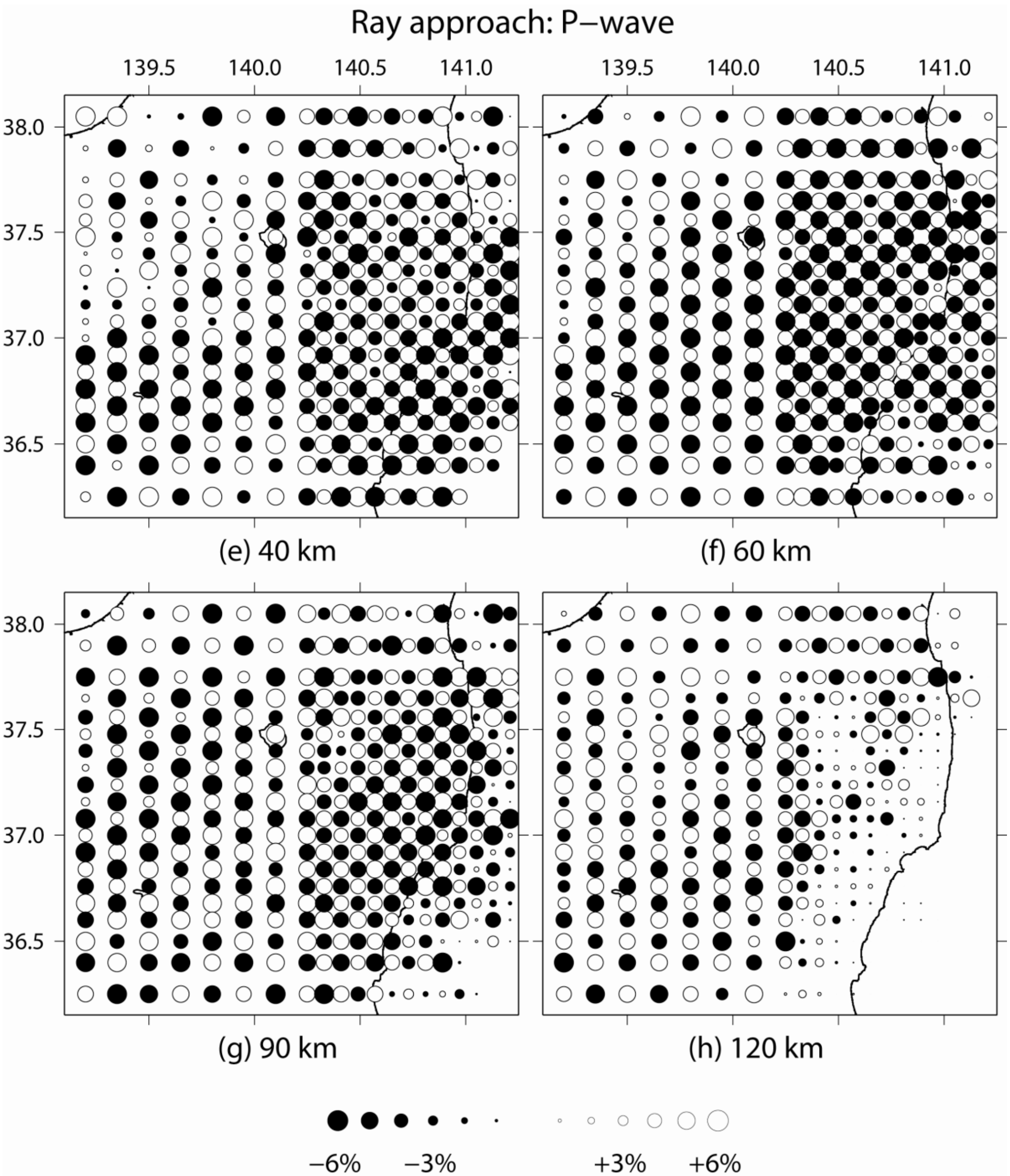

Figure S7. Ray approach results of a checkerboard resolution test for Vp structure at four representative depth layers in the upper mantle under the whole study area.

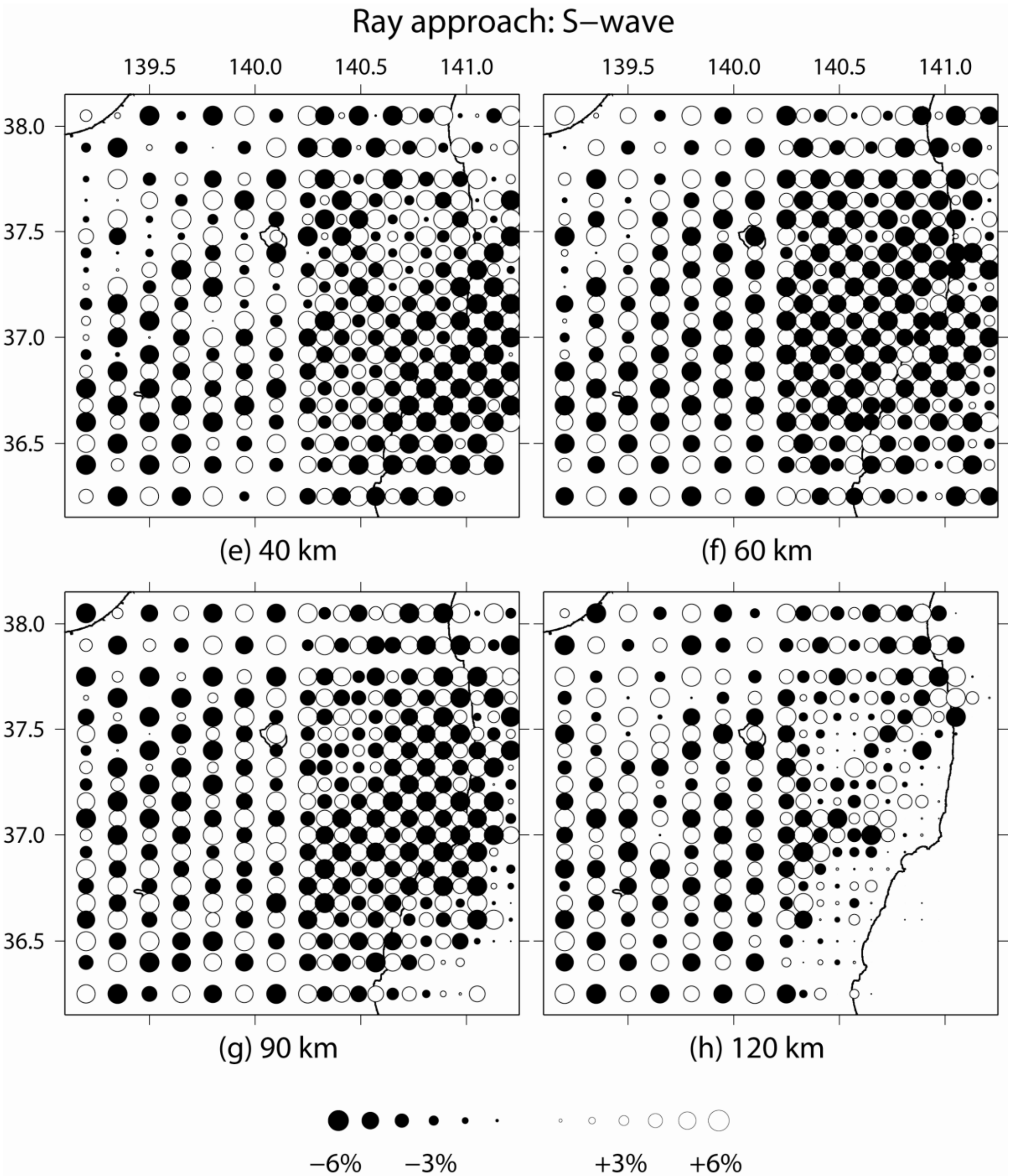

Figure S8. The same as Fig. S7 but for Vs structure.

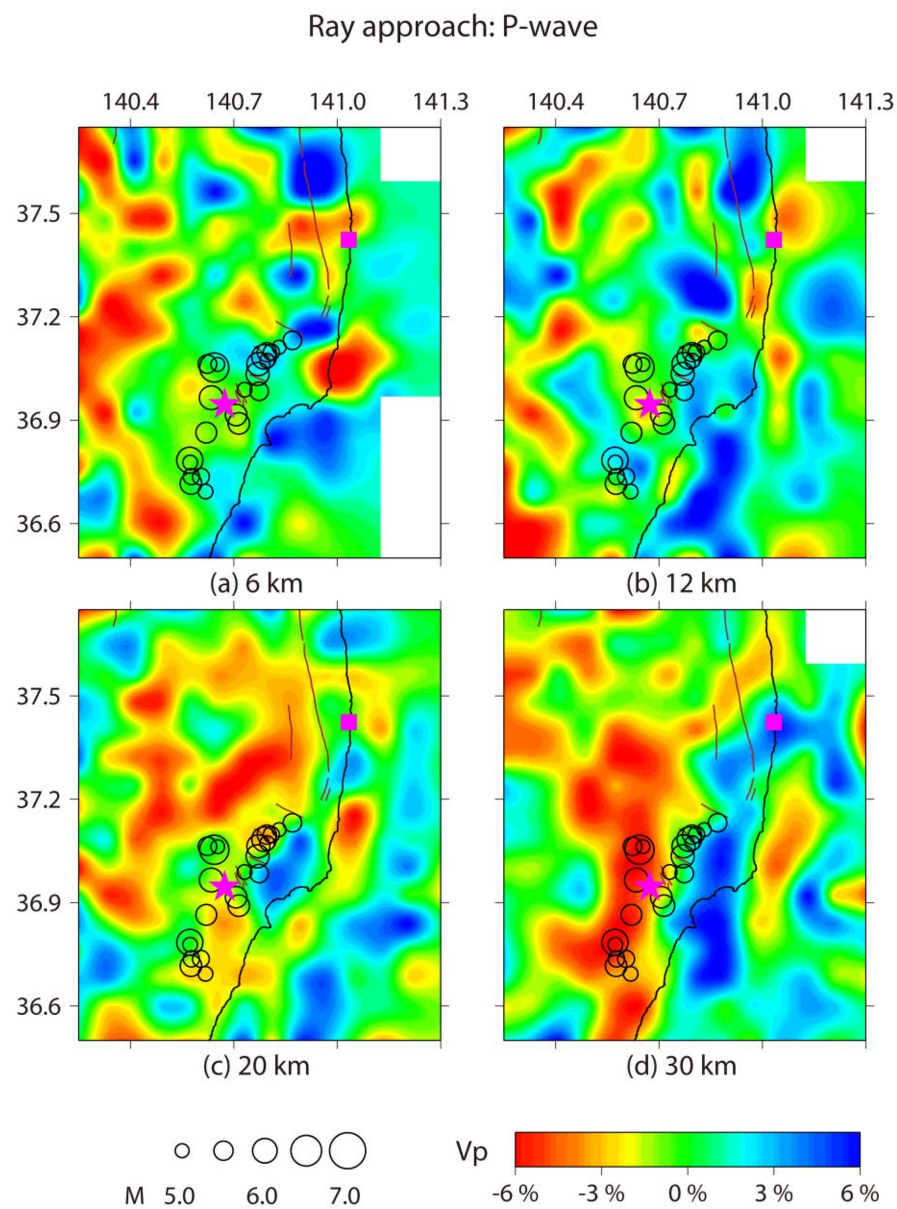

Figure S9. Map views of P-wave tomography with the ray approach in the crust under the Iwaki earthquake and Fukushima nuclear power plant area. The layer depth is shown below each map. Red and blue colors denote low and high velocities, respectively. The velocity perturbation (in %) scale is shown at the bottom. The brown lines denote the active faults.

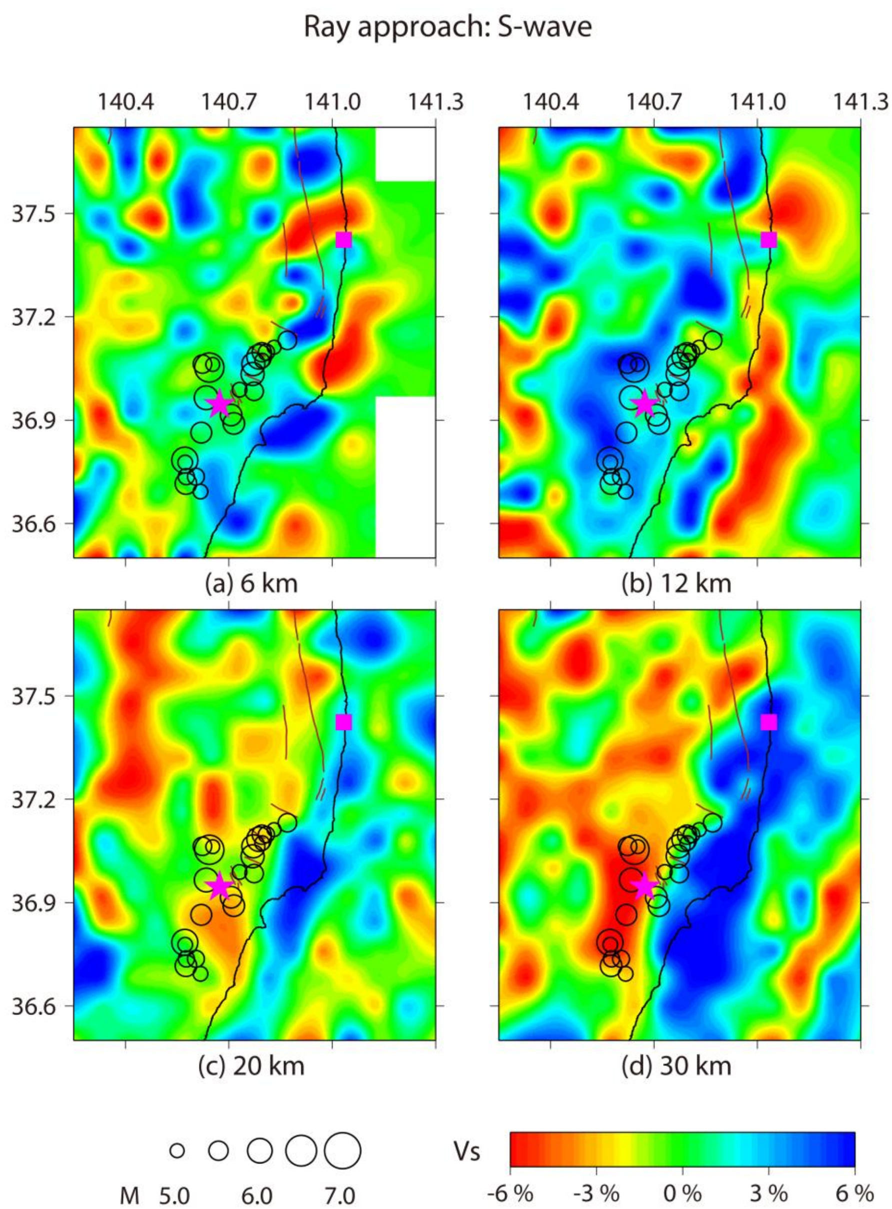

Figure S10. The same as Fig. S9 but for Vs structure.

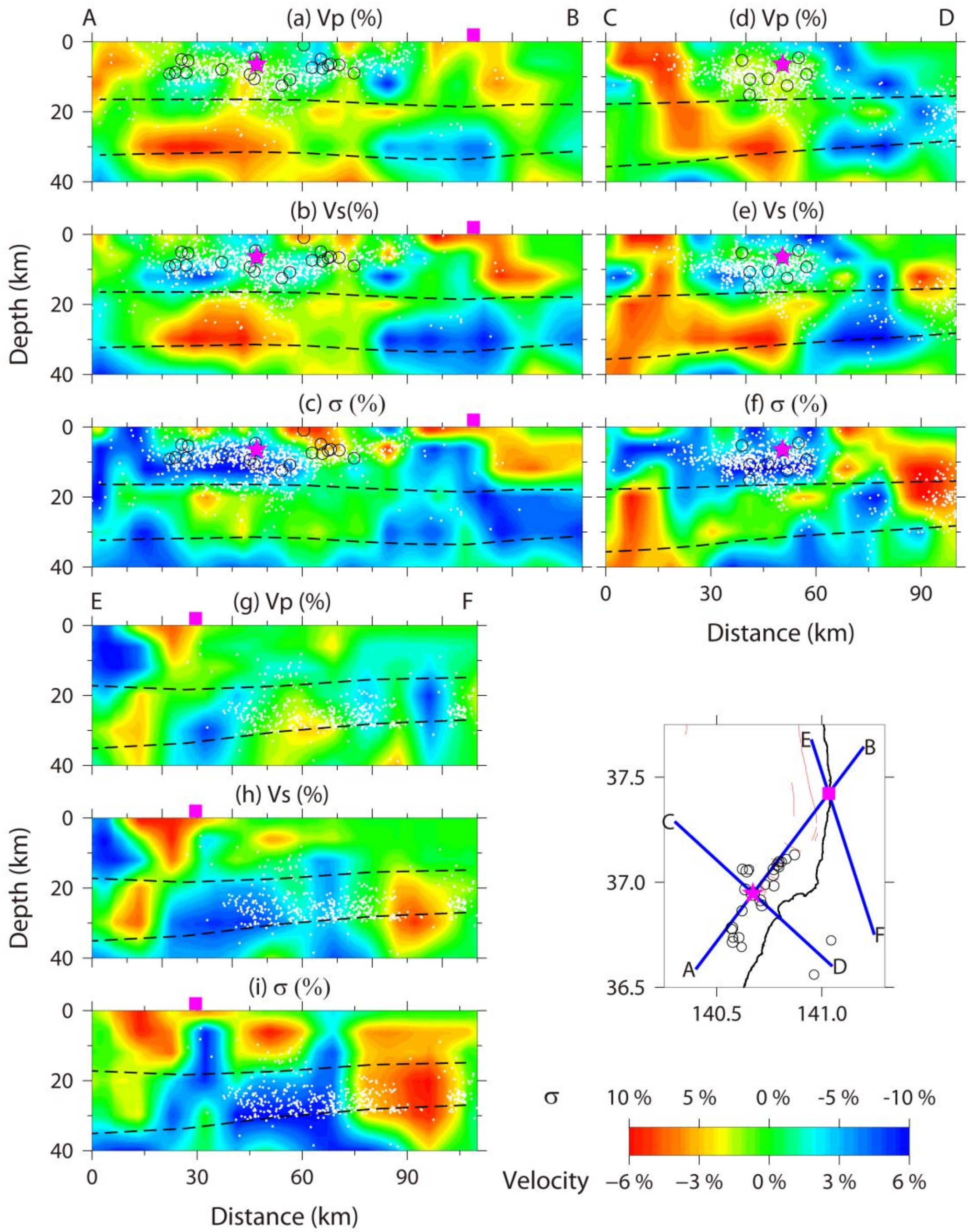

Figure S11. Vertical cross-sections of P-wave velocity, S-wave velocity, and Poisson's ratio images obtained with the ray tomography method along the lines AB (a-c), CD (d-f) and EF (g-i) as shown on the inset map. The vertical exaggeration is 1:1. Small white dots denote the events during 11 March 2011 to 27 October 2011, which are located within 8-km width along each line. The star symbol denotes the hypocenter of the Iwaki mainshock (M 7.0) with a focal depth of 6.4 km, while the open circles show the Iwaki aftershocks (M > 5.0). The square symbol represents the Fukushima nuclear power plant. The Conrad and the Moho discontinuities are shown in dashed lines.

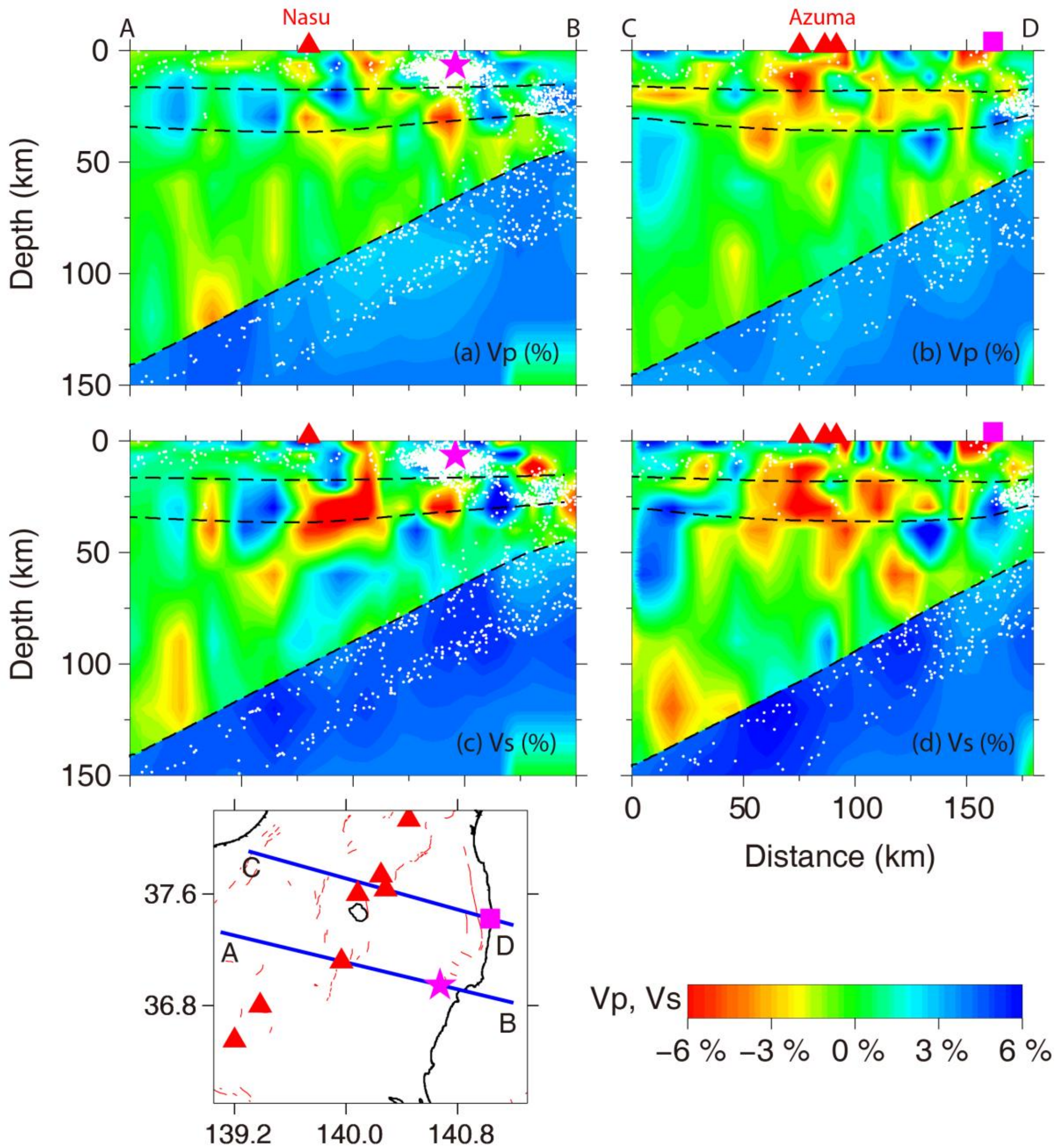

Figure S12. Vertical cross-sections of (a, b) P-wave and (c, d) S-wave velocity images along the lines AB and CD as shown on the inset map, which are determined with the ray tomography method. The vertical exaggeration is 1:1. Small white dots denote the events during 3 June 2002 to 27 October 2011, which are located within a 20-km width along each line. The star and square symbols denote the hypocenter of the Iwaki mainshock (M

7.0) and the Fukushima nuclear power plant, respectively. The triangle symbol represents the active volcanoes. The three dashed lines denote the Conrad and Moho discontinuities and the upper boundary of the subducting Pacific slab.

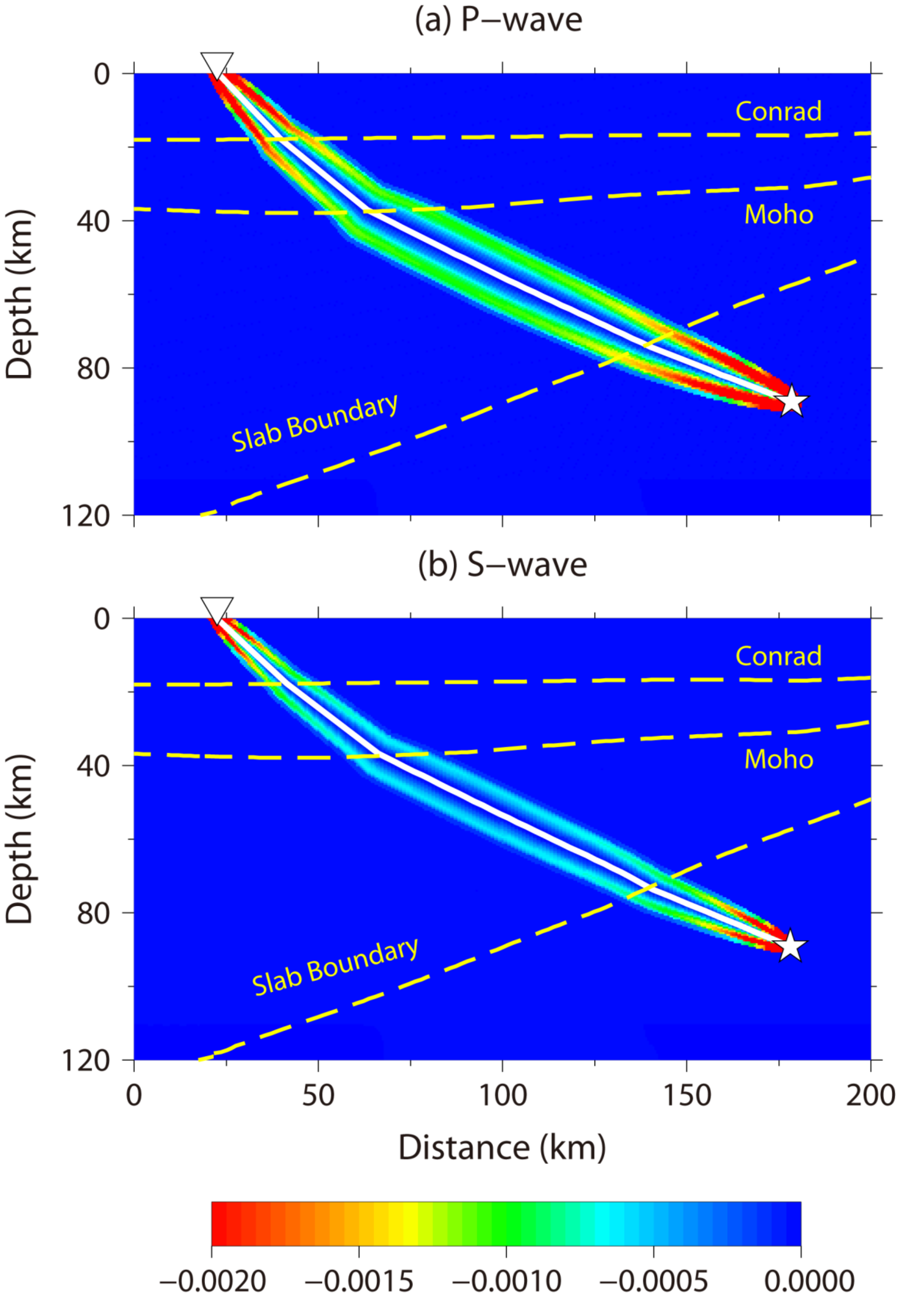

(a) P–wave
Conrad
Moho
Slab Boundary
Depth (km)
0
40
80
120
(b) S–wave
Conrad
Moho
Slab Boundary
Depth (km)
0
40
80
120
0
50
100
150
200
Distance (km)
−0.0020
−0.0015
−0.0010
−0.0005
0.0000

Figure S13. An example of (a) P and (b) S wave finite-frequency travel-time sensitivity kernels with a dominant frequency of 4.0 Hz. The earthquake (white star) is located within the subducted Pacific slab. The inverse triangle denotes the receiver. The curved white lines represent the geometrical ray paths. The yellow dashed lines show the Conrad and Moho discontinuities and the upper boundary of the subducted Pacific slab.